High Flux Thin-Film Nanocomposites with Embedded Boron Nitride Nanotubes for Nanofiltration

Serena Casanova,†‡ Tian-Yin Liu, § Yong-Min J. Chew,†‡ Andrew Livingston,§** Davide Mattia†‡*

†Department of Chemical Engineering, University of Bath, BA2 7AY, UK

‡Centre for Advanced Separations Engineering, University of Bath, BA2 7AY, UK

§Department of Chemical Engineering, Imperial College London, South Kensington Campus, SW7 2AZ, UK

**Department of Engineering and Material Sciences, Queen Mary University of London, London E1 4NS, UK

* Address correspondence to d.mattia@bath.ac.uk

Abstract

A novel thin film nanocomposite (TFN) membrane was obtained by incorporating boron nitride nanotubes (BNNTs) into a polyamide (PA) thin selective layer prepared via interfacial polymerisation. The addition of just 0.02 wt% of BNNTs led to a 4-fold increase in pure water permeance with no loss in rejection for divalent salts, methylene blue or humic acid compared to the pure PA membrane. Loadings higher than 0.02 wt% of BNNTs led to agglomeration with overall loss of performance. For the membranes containing 0.02 wt% BNNTs, the pure water permeance was 4.5 LMH@bar, with > 90% rejection of $MgSO_4$ and > 80% rejection of $CaCl_2$. Fouling tests with humic acid showed a flux recovery ratio of > 95% with ~50% lower flux loss during the fouling cycle compared to the polyamide only membrane. These values represent a significant improvement over both commercial polyamide membranes and TFN membranes incorporating carbon nanotubes. We assert that the very small quantity of BNNTs needed to produce the enhanced performance opens the way to their use in water treatment applications where nanofiltration membranes are subject to severe organic fouling.

Keywords: Boron nitride nanotubes; Chemical vapour deposition; Interfacial Polymerisation; Nanofiltration

1. Introduction

Polymeric nanofiltration (NF) membranes have become a mainstay of water treatment processes, with high recovery rates [1], facile modular scale up [2] and economic viability across a broad range of feed [3]. NF membranes are particularly effective for the combinatorial rejection of salts, organic compounds, natural organic matter (NOM), and dyes. [4]. Industry, however, still faces challenges including high energy costs per unit volume of water purified [5], handling of retentate waste [6], membrane fouling, and a fundamental understanding of the mechanisms underlying the purification of complex feeds [7].

Thin-film composite (TFC) membranes composed of a very thin, dense selective layer supported by a porous support combine high flux and rejection with mechanical stability. Although TFC membranes are successfully used commercially [8], there is still need to increase efficiency, reduce energy consumption and extend chemical stability [9]. Many approaches have been explored to improve the performance of TFCs, including diverse fabrication methods, and the tuning of precursors used to fabricate the membranes [10]. Another promising strategy is the incorporation of inorganic nanomaterials in the thin selective layer to form so-called thin-film nanocomposite (TFN) membranes [7]. Nanomaterial additions alter the structure of the selective layer by finely tuning properties such as hydrophilicity [11], porosity [12], surface zeta potential [13] and stability [14, 15]. Additionally, the nanomaterials can introduce desired features such as fouling resistance [16], adsorption [17] and photocatalytic characteristics [18] into the membranes.

Amongst the wide range of nanomaterials tested to date [2], carbon nanotubes (CNTs) have been considered for application in membrane technology due to their fast water transport and low tortuosity [19]. The reduced friction of water on the defect-free carbon surface in these nanotubes results in very high water permeances through the tubes [20], translating into higher efficiency (i.e. higher flux) per applied pressure [21]. However, efforts to create membranes with the CNTs aligned perpendicularly to the membrane's surface in a commercially scalable fashion have been have been, so far, unsuccessful [22-24]. On the other hand, the incorporation of randomly aligned CNTs in polymer matrices has led to the successful formation of selective membranes [25], but with only modest increases in water permeance and a decrease in selectivity [26, 27]. While the former can be attributed to the small fraction of tubes directly connecting feed and permeate, the latter is attributed to the formation of uncontrolled permeation pathways at the interface between the CNTs and the polymer, due to poor chemical

compatibility [28]. This aspect has been addressed by introducing an additional functionalisation step with acid groups, to form hydroxyl and carboxyl groups on the tube surface [29]. The functionalised CNTs have been added in relatively large amounts (1 wt% - 10 wt%), with a corresponding increase in rejection of up to 5% and providing permeances up to 50% higher than those of the starting polyamide membrane [30, 31]. CNTs have also been functionalised with more complex zwitterion groups. However, these have penalised the water permeance when compared to pristine CNTs, though improving the rejection of NaCl from 97.6% to 98.5% thanks to the steric hindrance of the zwitterion functional groups [32]. Despite these promising results, the potential for permeance increase is limited by the low loadings of hydrophobic nanomaterials that can be incorporated into the membrane matrix before the onset of agglomeration, which leads to the formation of pinholes, with a subsequent loss of performance [33].

Herein, boron nitride nanotubes (BNNTs) are investigated as nanomaterials for TFN fabrication. We speculate that their physico-chemical characteristics will overcome some of the limitations of CNT-based TFNs highlighted above. Hexagonal BNNTs (*h*BN) are isostructural to graphitic CNTs, but behaving as electrical insulators and showing higher resistance to oxidation [34]. Molecular dynamics simulations on BNNTs in the subcontinuum range, with diameters 0.8 nm, have shown faster pure water flux than in CNTs [35]. For such small diameters it was shown that increased van der Waals and electrostatic interactions between the nanotube walls and the water molecules contribute to an easier filling of the bore of BNNTs than for CNTs [36]. However, when the diameters of the tubes studied were larger, CNTs outperformed BNNTs in terms of improved water fluxes [37]. This was ascribed to differences in the electronic landscape in the two nanotube walls [38]. Simulations also showed that BNNTs have tunable cation and anion selective properties due to the partial charge on the boron and nitrogen atoms of the nanotube [39] and osmotic energy storage capabilities [40]. Additionally, when boron nitride nanosheets were recently embedded in mixed matrix membranes, they showed improved fouling resistance [26]. Boron nitride nanotubes have recently been used to fabricate ultrafiltration membranes with improved thermal resistance and mechanical stability [41]. Moreover, CNTs have been shown to have antioxidant capabilities that slow down chlorine attack on polymeric membranes [28], however this effect is as yet unreported for BNNTs. Using BNNTs as membrane nanofillers is motivated, together with its novelty, by the fact that materials with high negative zeta potentials allow for rejection of pollutants not only by size but also by charge [42].

Despite the many potential advantages of BNNTs over CNTs, there has been notably less published research on BNNTs than on their carbon counterparts, attributed mainly to the lack of methods for the production of BNNTs at scale [34]. This obstacle has been overcome in this work, optimising a known technique [43] for the production of BNNTs by chemical vapour deposition (CVD). The nanomaterial was then embedded in the selective phase of an interfacially polymerised polyamide (PA-BNNT) membrane. BN is negatively charged in water over a broad pH range [44] and can adsorb OH^- on its surface further increasing its negative charge [40].

2. Materials and Methods

2.1 Materials

Boron (B, ≥ 95%), magnesium oxide (MgO, ≥ 99.99%), iron oxide (Fe_2O_3, ≥ 99.9%) and MgO nanopowder (average particle size ≤ 50 nm, measured by BET [45]) were purchased from Sigma Aldrich. Ethanol (≥ 99%) was purchased from Fisher Scientific. P-type silicon wafers polished on one side were purchased by Agar Scientific. Hydrochloric acid (38%) was purchased from Sigma Aldrich. Commercial polyether sulfone (PES) membrane Microdyn Nadir PMUP010 with 10 kDa nominal molecular weight cut-off was purchased from Steriltech. Deionised (DI) water was used unless specified otherwise. Methanol (MeOH, anhydrous, 99.8%), Piperazine (PIP, 99%) ReagentPlus®, with MW86, n-hexane (anhydrous, 95%) and trimesoyl chloride (TMC, 99%) were purchased from Sigma Aldrich. Diiodomethane (DIM, 99%) was purchased from Sigma Aldrich. Salts (*e.g.*, NaCl, $CaCl_2$ and $MgSO_4$) were purchased from Sigma Aldrich. Sodium hypochlorite technical solution was purchased from Fischer Scientific.

2.2 BNNTs synthesis

BNNTs synthesis (Fig. 1) with ammonia gas and boron powder precursors was catalysed by Fe_2O_3 and MgO catalysts with a molar ratio of B:MgO:Fe_2O_3 = 2:1:1. B, MgO and Fe_2O_3 were pre-mixed at 250 r.p.m. for 12 h in a Fritsch Pulverisette P6 planetary ball mill, half filling a 45 ml stainless steel grinding bowl with 2.2 g of B, MgO and Fe_2O_3 in an ethanol suspension and 18 grinding balls with 5 mm diameter. After ball milling, 5 ml of precursor was poured in a Coors™ alumina combustion boat, which was then capped with a silicon wafer previously seeded with MgO nanopowder. The closed boat was then placed in a 15 cm long quartz test

tube (ID 18 mm, OD 19 mm) facing the gas inlet in the centre of a quartz tube reactor (H-Baumbach, ID 20 mm, OD 22 mm) in a three sections horizontal TZF 12/38/850 type CARBOLITE tubular furnace. Temperatures inside the furnace were monitored by external thermocouples. Gas flows were controlled with Omega FMA 5400A/5500A series mass flow controllers (MFCs) regulated by a LabVIEW program. The tube reactor was abundantly flushed with Ar and then let ramp up at 10 °C/min up to 1100 °C under a 200 sccm Ar flow. Then, the gas flow was switched to 145 sccm NH_3 and the temperature increased to 1200 °C at the same heating rate. This maximum temperature was kept for 1 hour before letting the system cool down to room temperature under a 200 sccm Ar stream. The exhaust NH_3 gas was neutralized with a sulphuric acid scrubber, generating ammonium sulphate salts. The BN nanotubes white powder was gently removed with a stainless steel spatula by scratching it from the silicon substrate and boat top and sides. The unreacted boron in the collected white powder was removed in air at 700 °C for 2 hours, where it reacted to form boric anhydrite vapour. BNNTs have high thermal stability and are resistant to oxidation up to 950 °C [45]. Catalysts were removed with a 3 hours 10% HCl (purity 36.5-38.0%, purchased from Sigma Aldrich) water cleaning at 40 °C, followed by washing of the products in DI water by vacuum filtration using a 0.45 µm pore size nylon membrane (Pall Corporation).

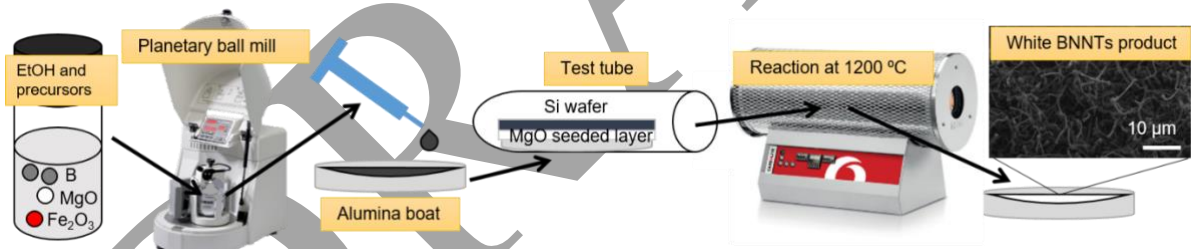

Fig. 1 Schematic of the CVD of boron nitride nanotubes production.

2.3 Polyamide membrane fabrication

The PA-BNNTs membranes were synthesized by interfacial polymerisation following an established vacuum filtration technique [46], which has been recently used for the fabrication of nanocomposite membranes [47]. The PES support membrane (Microdyn Nadir PMUP010) was cut in discs with 5.5 cm in diameter, and then flushed with 20 ml of water in a filtration setup prior to synthesis. Then, 1 wt% PIP aqueous solution (MeOH:H_2O 50:50 v/v%) solution was prepared by rapidly dissolving the PIP flakes. For the PA-BNNT membranes, 0.01, 0.02 or 0.03 wt% BNNTs were dispersed in the amine solution by ultrasonication for 1 h (Table 1). Then, 25 ml amine solution or amine solution with dispersed BNNT was pumped through the

support membrane until the entire amount of solution was filtered, while ensuring the membrane remained wet. Subsequently, any residual drops on the side of the wetted membrane were removed by using an air gun to avoid the formation of defects in the resulted amine-rich film. In the interfacial polymerisation, a 0.8 wt% TMC n-hexane solution statically contacted the amine-saturated support in the filtration setup. The reaction time was 3 min. The residual organic solution was discarded, and the membrane was quenched with n-hexane for 1 min. After reaction, the membrane was left to dry at room temperature for 24 h. Similarly, a thin film was formed by contacting 1 ml of PIP solution with 1ml of TMC solution, specifically for the analysis of a free standing film at the interface.

Membranes with different concentration of BNNTs in the starting solution were prepared; their nomenclature, PIP solution composition, and the estimated weight of nanofiller deposited per unit area by filtering 25 ml of amine solution are reported in Table 1. The concentrations to be investigated were chosen in a range where no obvious large agglomeration could be observed on the membrane top surface with the naked eye. It should be noted that there is an uncertainty in the estimation of the amount of BNNTs per unit area, due to the possibility that some minor fraction of nanomaterial filtered through the PES support.

Table 1 Composition of the PIP solutions in MeOH:H_2O 50:50 v/v% for the PA-BNNTs membranes.

Membrane	PIP (wt%)	MeOH/H_2O (wt%)	BNNTs (wt%)	c_S (mg/cm2)
PA-BARE	1.00	99.00	0.00	0.000
PA-BNNTs0.01	1.00	98.99	0.01	0.096
PA-BNNTs0.02	1.00	98.98	0.02	0.193
PA-BNNTs0.03	1.00	98.97	0.03	0.283

2.4 Characterisation of BNNTs powders

The produced nanotubes were coated with 5 nm of chromium and positioned on carbon tape for analysis with a JEOL JSM-6301F FESEM at 5kV. JEOL JSM-2100Plus TEM samples were prepared by dispersing the nanotubes in ethanol. Two to five drops of the sample were then placed on a TEM window (Lacey carbon purchased from EM Resolutions) until a desirable concentration was reached. Analysis of structural features with ImageJ was done on a minimum of 10 measurements. Optical Images of the substrates with BNNTs grown on them were taken with a Digital Microscope VHX-6000 series. Raman spectroscopy was carried out on the as-synthesized samples on a glass slide in a Renishaw Raman Microscope series 1000 using a frequency-doubled argon ion laser (wavelength 244 cm-1, 5.08 eV) with spectral resolution of

5 - 10 cm^{-1} and a 40 × UV objective lens. XRD tests of products of the synthesis were reduced into fine powders dispersed on a silicon wafer were carried on 1 mg of product with a Bruker D8 Advance for $10 < 2\theta < 70$ with a Vantec detector with Cu K-alpha radiation.

XPS was performed on powdered BNNTs samples using a Thermo Fisher Scientific K-alpha+ spectrometer. Samples were analysed using a micro-focused monochromatic Al x-ray source (72 W) over an area of approximately 400 microns. Data was recorded at pass energies of 150 eV for survey scans and 40 eV for high resolution scan with 1 eV and 0.1 eV step sizes respectively. Charge neutralisation of the sample was achieved using a combination of both low energy electrons and argon ions. Data analysis was performed in CasaXPS using a Shirley type background and Scofield cross sections, with an energy dependence of -0.6.

2.5 Polyamide membrane characterisation

Membranes were coated with 10 nm of Cr before imaging in a JEOL JSM-6301F FESEM. Micrographs were taken at 5kV. Atomic Force Microscopy (AFM) Nanosurf EasyScan 2 Flex scans were taken by using the Dynamic Force Mode with a 190Al-G tip on areas 5 µm × 5 µm with 256 points/line. The data was analysed with Gwyddyion and the software's internal functions were used to assess the membrane's average roughness (R_a). Dataphysics Optical Contact Angle (OCA) Measuring Device with 0.5 µl wetting liquid drops was also used to characterise the membranes. The Young's contact angle (θ_Y) on a flat smooth surface is related to the measured contact angle (θ_W) via the Wenzel equation [48]:

$$cos\theta_W = r\, cos\theta_Y, \quad (1)$$

where r is the ratio between the membrane surface area and the projected area, obtained by AFM.

The surface zeta potential of samples with dimensions 2 × 1 cm or 1 × 1 cm was measured in a SurPASS electrokinetic analyser with adjustable gap cell in a pH range between 3 and 10. For each pH value, the measurement was repeated four times. A Perkin Elmer Spectrum FTIR-ATR Spectrometer was used to characterise the membranes' selective layer surface, with 16 scans per run between 600 and 4000 cm^{-1} and a spatial resolution of 2 cm^{-1}.

Sections of the polyamide membranes top surface measuring 1 cm × 1 cm were also analysed by XPS. The ratio O/N from the XPS analysis was measured to assess the degree of crosslinking in relation to loading percentage. This was calculated from

$$crosslinking\ (\%) = \left(\frac{(O/N)_{XPS} - (O/N)_{fully\ cross-linked}}{(O/N)_{fully\ linear} - (O/N)_{fully\ cross-linked}}\right), \quad (2)$$

where $(O/N)_{XPS}$ is the oxygen to nitrogen ratio obtained experimentally, neglecting the 398 eV contribution of the *h*BN nitrogen [49]. $(O/N)_{fully\ linear}$ and $(O/N)_{fully\ crosslinked}$ are the ratios for a fully linear and fully crosslinked polyamide, respectively [50].

Phillips CM200 TWIN TEM samples were prepared by gently depositing a thin film on a TEM window and imaging it at 250 and 25k magnification.

2.6 Membrane filtration performance

Pure water flow was tested in cross flow mode (schematics in [26]) on a minimum of three membranes per composition, with 24 h of compaction at 7 bar and three days of testing at 3 bar.

Dye and salts rejection was tested for 7 h with a 45 L h^{-1} pump flow rate. Rejection of methylene blue was assessed using a UV spectrophotometer (UV Cary 100, Agilent, U.K.), while rejection of the salts was measured using an Orion Versastar ThermoScientific conductivity meter. The feed concentration for the dye tests was 0.01 g L^{-1}, whilst for salts rejection it ranged from 500 to 2000 ppm.

Humic acid fouling tests were performed on pre-compacted membranes in cross flow mode. The 2.5 L feed of 1 g L^{-1} humic acid in water was prepared beforehand and mixed with a magnetic stirrer for 24 hours before the test. The fouling test consisted of two fouling cycles of 15 hours and two cleaning cycles of one hour each. The flow rate was set as 175 ml min^{-1} (Reynolds number, *Re* = 130) and 750 ml/min (*Re* = 550) for fouling and cleaning respectively. Flux recovery ratio (FRR) was measured before each cycle as follows:

$$FRR\ (\%) = \left(\frac{J_{AF}}{J_{BF}}\right) \times 100\ , \quad (3)$$

where J_{BF} and J_{AF} are the two fluxes before fouling and after cleaning, calculated for each cycle.

The membrane total resistance (R_t) after 15 hours of fouling test was also calculated:

$$R_t = R_m + R_r + R_{ir}, \quad (4)$$

with R_m, R_r and R_{ir} being the intrinsic membrane resistance and the reversible and irreversible fouling resistance, respectively. These are calculated by using:

$$R_m = \frac{\Delta P}{\mu \times J_{BF}}; \tag{5}$$

$$R_{ir} = \frac{\Delta P}{\mu \times J_{AF}} - R_m; \tag{6}$$

$$R_r = \frac{\Delta P}{\mu \times J_F} - R_m - R_{ir}. \tag{7}$$

The transmembrane pressure is indicated with ΔP and the viscosity with μ, while J_F is the flux in $m^3 s^{-1}$ of humic acid after 15 hours of fouling. The term $R_{\%}$ was used to assess the extent of reversible fouling in each membrane during fouling tests:

$$R_{\%} = \frac{R_r}{R_t} \times 100. \tag{8}$$

The first 10 ml of permeate were discarded in every test, to account for dead volume and permeate tubing. The mass balance for the rejection of component i is so calculated:

$$mass\ balance\ (\%) = \frac{V_{P,i}c_{P,i} + V_{R,i}c_{R,i}}{V_{F,i}c_{F,i}} \times 100\,, \tag{9}$$

where the subscripts P, R and F stand for permeate, feed and retentate respectively; V is the volume and c the concentration.

Chlorine resistance tests were performed with 4 L feed water containing 2000 ppm NaOCl and 2000 ppm $CaCl_2$. Rejection and permeance were monitored over a period of 5 hours and 30 minutes, while the membranes were tested in cross flow mode with a pump velocity of 45 L h^{-1} at 3 bar. Membranes were pre-compacted before rejection tests.

3. Results and Discussion

3.1 BNNTs synthesis

BNNTs were synthesized via chemical vapour deposition, resulting in a dense product (Fig. 2a), with the BNNTs having open ends (Fig. 2b) and homogenously grown over the entire substrate area (Fig. 2c) with a vertical orientation (inset cross-sectional HRTEM). The BNNTs powder was collected with a yield of ~10 mg per run by simple scratching of the silicon wafer (W x L 14 x 70 mm) substrate. The diffraction pattern generated by a single tube (Fig. 2d) confirmed the *h*BN (002) crystal structure of boron nitride multiwalled (wall thickness ~4.5 nm) nanotubes [51], with a straight inner channel of *c.a.* 8 nm in diameter and an outer diameter of *c.a.* 17 nm (Fig. 2e) where the interspace layer distance of *h*BN is 0.328 nm as expected from literature [34]. Combining the open ends and penetrating inner voids, the as-synthesized BNNTs are ideal candidates for creating nanoscale channels in TFN membranes [52]. The morphology of the BNNTs showed a relatively wide size distribution with outer diameters in the range of 5 to 105 nm and tube lengths in the range of 1 to 5 μm, as statistically counted by 200 tubes in TEM micrographs (Fig. 2f).

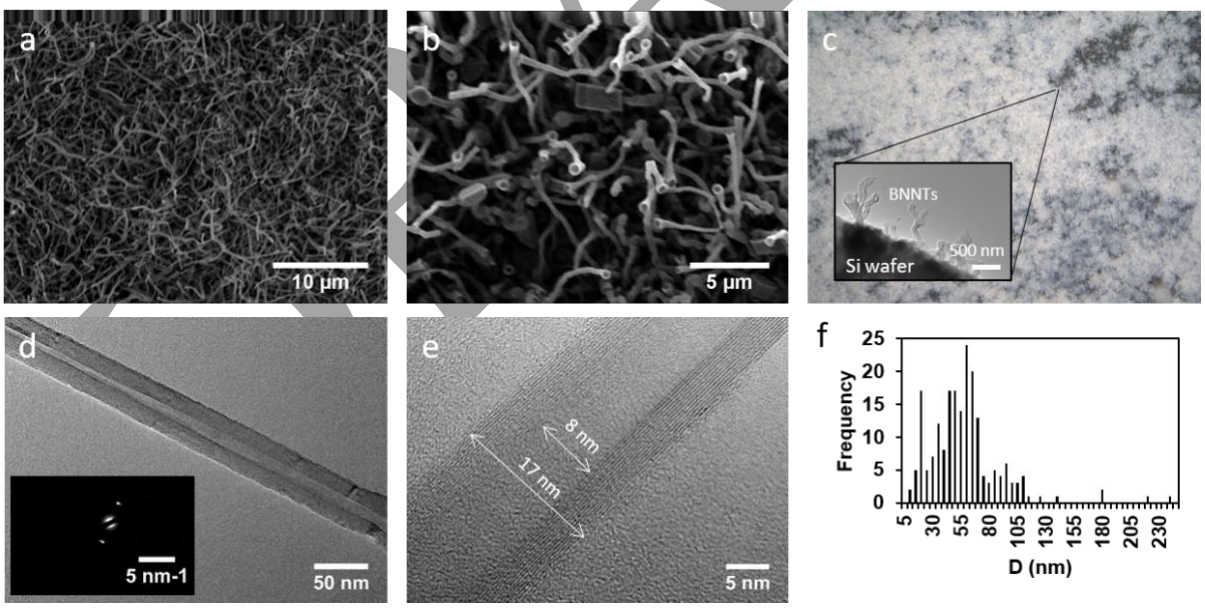

Fig. 2 (a) FESEM micrograph of BNNTs on the Si wafer taken at 3000 x magnification and **(b)** collected from the alumina boat taken at 5000 x magnification with 8 mm working distance. **(c)** Optical microscope image (500 x) with a TEM micrograph inset showing BNNTs grown on a piece of silicon wafer; TEM micrographs and **(d)** corresponding diffraction pattern and **(e)** measures for inner and outer tube diameter of a selected BNNT tube where the *h*BN interlayer spacing can be observed. **(f)** Counts of outer diameter intervals for 200 tubes randomly imaged with TEM.

The BNNTs powder samples present the typical Raman *h*BN peak at 1369 cm^{-1} (Fig. 3a). The XRD spectra in Fig. 3b shows four main BN peaks at $2\theta = 10.5^{o}$ (*h*BN 001), 29^{o} (*h*BN 002), 40^{o} (*h*BN 100) and 53^{o} (*h*BN 004) [53], alongside some iron and MgO peaks in the region $20^{o} < 2\theta < 40^{o}$, identified as catalyst impurities. Boron nitride FTIR peaks are identified in Fig. 3c for the vibration mode along the tubes' longitudinal axis at 1367 cm^{-1}, in the tangential direction at 1537 cm^{-1} and the out of plane buckling mode at 795 cm^{-1} [43]. The spectra also presents peaks attributed to Si-O in the 1130-1000 cm^{-1} region and Si-H in the 850-900 cm^{-1} region, as the spectra was taken before the BNNTs material was scraped from the Si substrate. XPS results (Fig. 3d) identify a B/N atomic ratio of 1.18 in the powder BNNT sample, very close to the theoretical value of 1. Peaks for *h*BN are identified at 190.41 eV and 398.00 eV for B and N respectively, and a 3.75 at.% of N-B-O bonds can be observed in the B high resolution spectra [49].

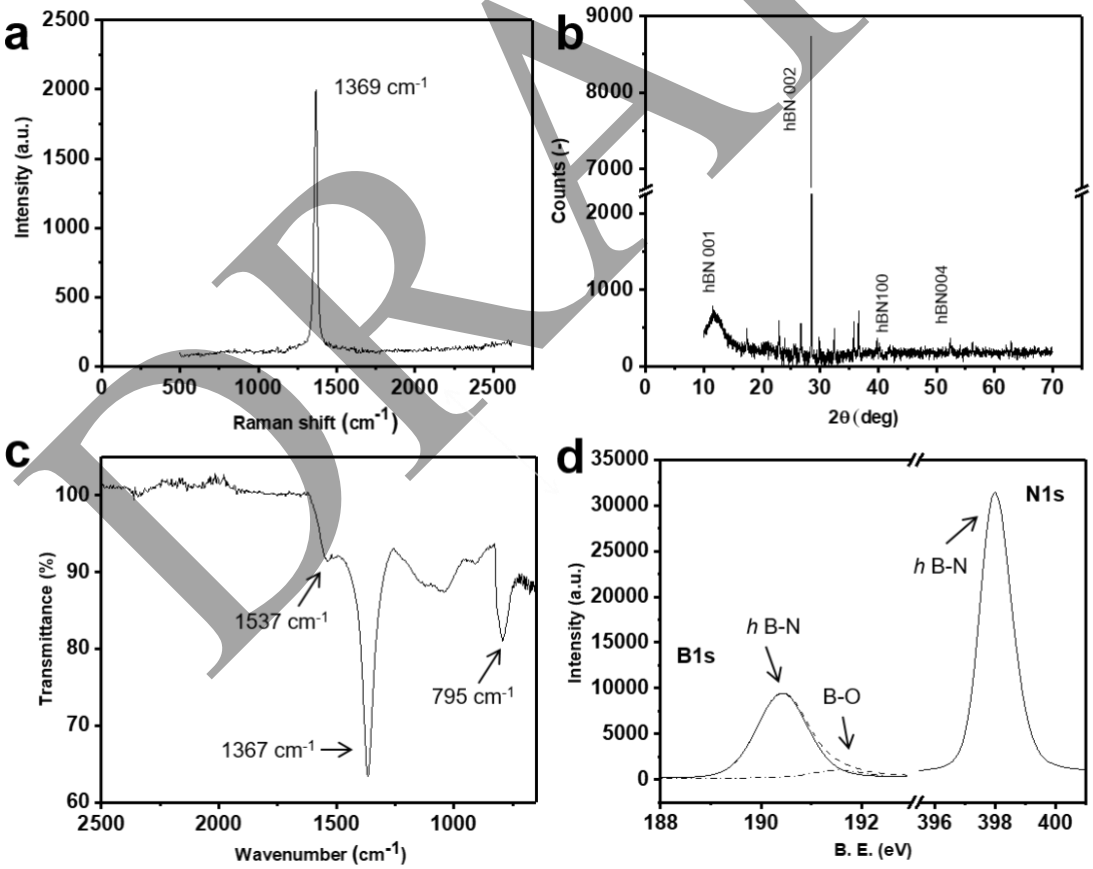

Fig. 3 (a) Raman analysis of BNNTs with the characteristic *h*BN peak at 1369 cm^{-1} and **(b)** XRD pattern of the as produced BNNTs powder, showing four characteristic *h*BN peaks; **(c)** FTIR of BNNTs on silicon wafer; and **(d)** B1s and N1s high resolution XPS spectra of the BNNTs.

3.2 Characterisation of PA-BNNTs membranes

The surface and cross-sectional morphologies of the produced polyamide membranes are shown in Fig. 4. The irregular morphology increased with BNNTs loading, which is consistent with an increase in the average surface roughness (R_a, nm) in Table 2, and therefore the ratio between the membrane surface area and the projected area, r, and morphological changes measured by AFM (Fig. 5). The crumpled areas observed in the PA-BNNTs membranes showed similar material stiffness as the rest of the membrane (see phase plot analysis in **Error! Reference source not found.**), indicating that no BNNTs protrude out of the membrane from the top surface.

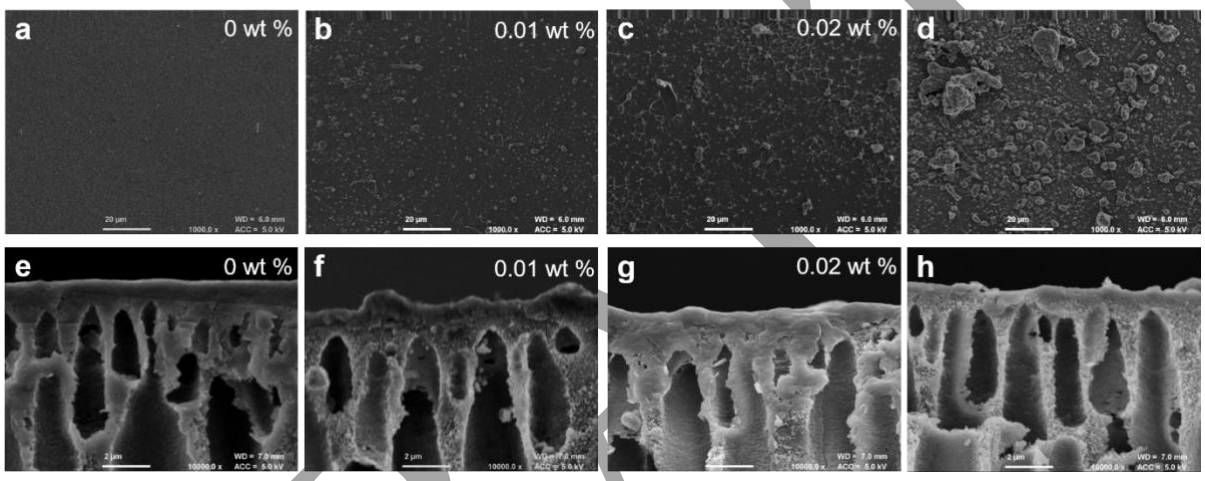

Fig. 4 FESEM top and cross section of membranes prepared from solutions containing different percentages of nanofiller: **(a,e)** bare, **(b,f)** 0.01 wt%, **(c,g)** 0.02 wt% and **(d,h)** 0.03 wt% PA-BNNTs membranes.

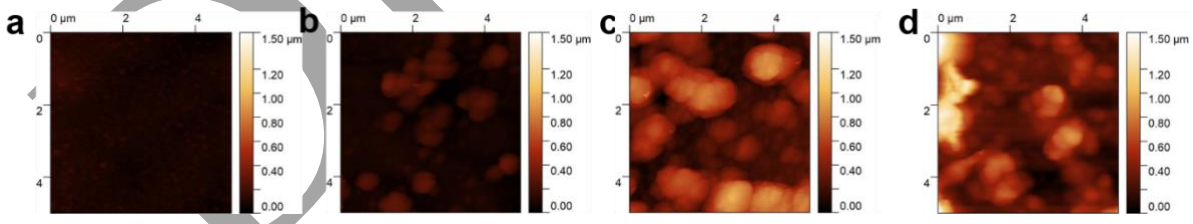

Fig. 5 AFM maps of membranes **(a)** bare, **(b)** 0.01 wt%, **(c)** 0.02 wt% and **(d)** 0.03 wt% PA-BNNTs membranes.

Measured contact angle varies as a function of BNNTs concentration (Table 2). Water contact angle increases by approximately 20o from PA-BARE to PA-BNNTs0.03, in agreement with both the increase in roughness R_a already observed in Fig. 5 and an observed reduced material hydrophilicity. When the measured contact angle and roughness are used to calculate values for the Young's contact angles *via* the Wenzel equation [48], an observable although not drastic increase in material hydrophilicity is observed, with Young's water contact angles increasing

by 15-20% for each 0.01 wt% of BNNT added. In contrast, the non-polar diiodomethane contact angle (θ_{Y_DIM}) decreased over the four membranes tested, in line with the loss of hydrophilicity of the membrane.

Table 2 Measured water (θ_{WATER}) and diiodomehtane (θ_{DIM}) contact angles, Young water (θ_{Y_WATER}) and diiodomehtane (θ_{Y_DIM}) contact angles obtained applying the Wenzel equation, average surface roughness R_a results on PA-BARE and PA-BNNTs membranes and ratio r between the membrane surface area and the projected area, obtained by AFM.

Membrane	θ_{WATER}	θ_{DIM}	θ_{Y_WATER}	θ_{Y_DIM}	R_a	r
	(deg, ± 2º)				(nm)	(-)
PA-BARE	25	30	35	39	19	1.11
PA-BNNTs0.01	32	29	40	38	49	1.11
PA-BNNTs0.02	30	28	49	48	172	1.32
PA-BNNTs0.03	45	10	59	44	181	1.37

A free-standing film was placed in the TEM to observe the embedment of the BNNTs in the polyamide (Fig. 6a). Wrinkles in the thin layer are created when this is transferred to the TEM grid, but these formations can be clearly differentiated from the BNNTs as these show a hollow nature as previously shown in Fig. 2 d,e and in the inset of Fig. 6a. Fig. 6b shows a picture of the polyamide thin film formed at the interface between the PIP H_2O/MeOH solution and TMC in hexane solution.

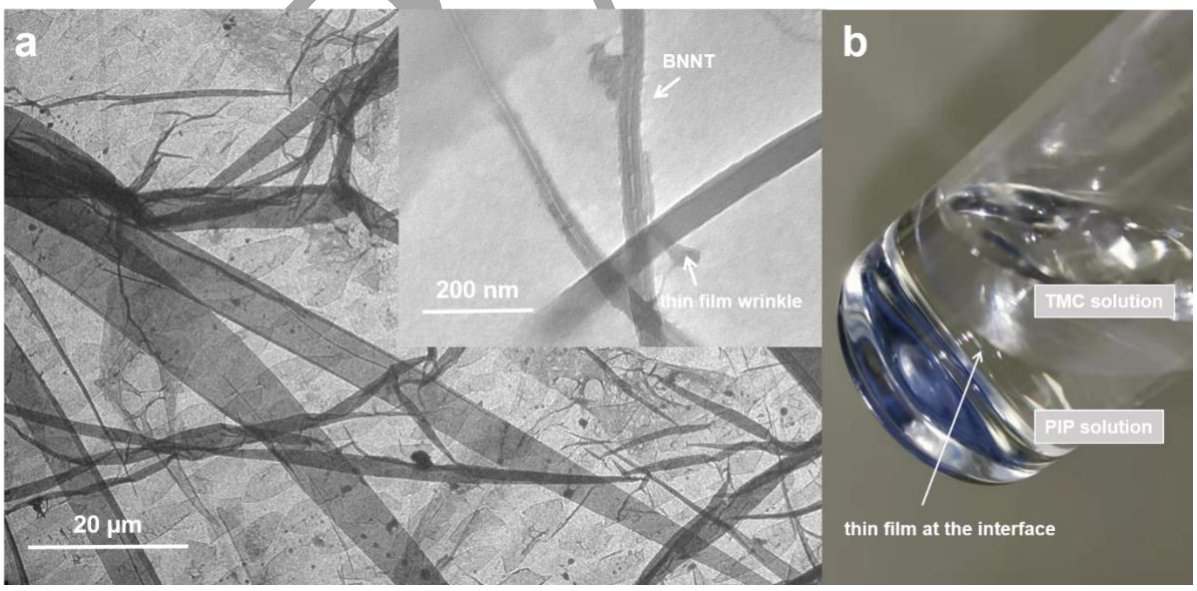

Fig. 6 (a) TEM micrograph of a free-standing film loaded with 0.01wt% BNNTs, observable in the magnified inset. Wrinkles generate in the film when it is transferred to the TEM grid. **(b)** Picture of a thin film produced at the interface between the TMC and PIP solutions.

As expected, the introduction of a negatively charged material in the texture of the IP membrane slightly decreased its surface zeta potential (Fig. 7). Although statistically significant (p-value=0.002), this change is not as dramatic as might be expected by the introduction of negatively charged nanomaterial, leading to the hypothesis that the vast majority of nanomaterial particles are surrounded by the selective polymer layer, and do not protrude from the top surface, consistent with the top layer stiffness results in **Error! Reference source not found.**.

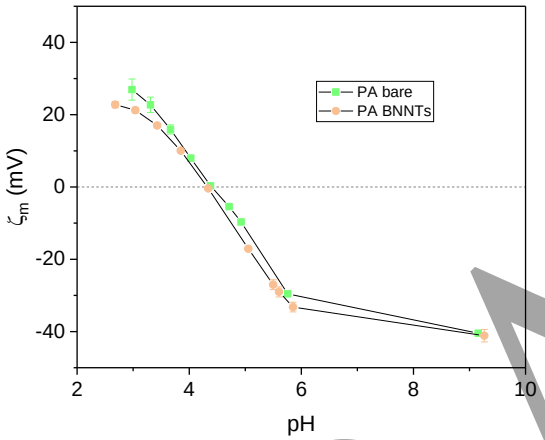

Fig. 7 Surface zeta potential (ζ_m) vs. pH of a PA-BARE (IEP=4.40) and PA-BNNTs0.01 (IEP=4.32).

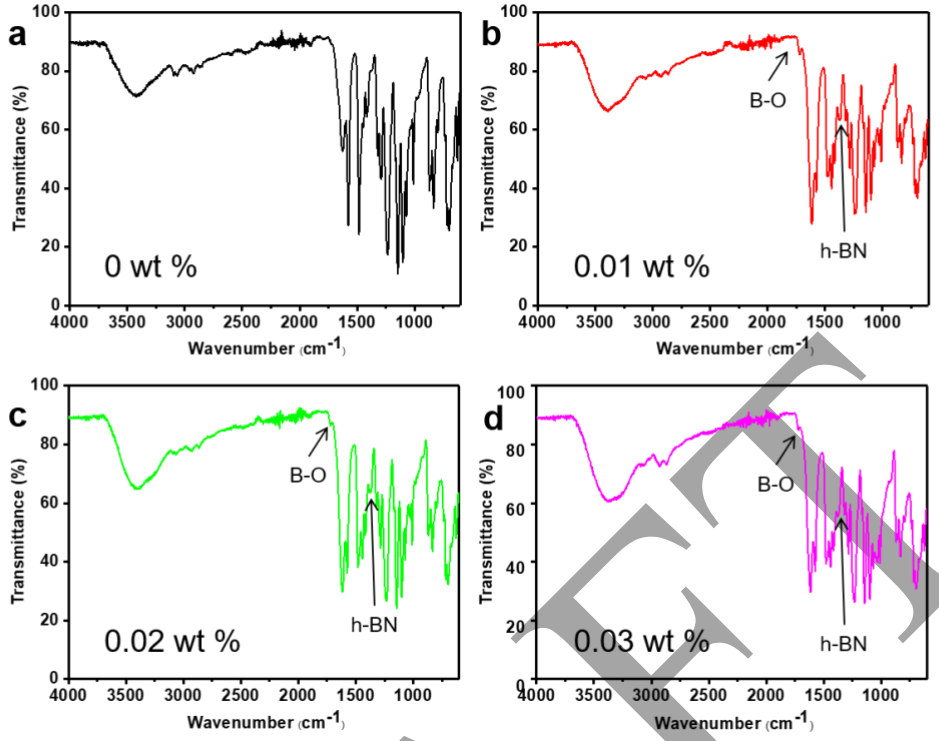

Fig. 8 FTIR spectra for (a) bare, (b) 0.01 wt%, (c) 0.02 wt% and (d) 0.03 wt% PA-BNNTs membranes.

Fig. 8a reports the FTIR-ATR spectra for the IP BARE membrane [54], and Fig. 8b-c the scans for membranes with increasing BNNT loading. The beam penetrates the sample for 0.5 - 2 µm during testing [55], therefore representing the whole thickness of the membrane top layer and not just the very top surface. Thus, at the highest BNNTs concentration, the predominance of the 1375 cm^{-1} BNNT' peak, corresponding to the longitudinal vibration mode of the tube, is observed [43, 56], together with a B-O functionalisation peak at 1721 cm^{-1} [57], showing a new bond not observable in the FTIR for the BNNTs in powder form (Fig. 3c), and potentially indicating some interaction between the boron nitride and the polymeric matrix already visible for BNNTs concentrations of 0.01wt.%.

The O/N ratio for each membrane is reported in Table 3. A fully cross-linked polyamide, $(O/N)_{fully\ cross-linked}$, has a *O*/*N* ratio of 1 and a theoretically fully linear polyamide, $(O/N)_{fully\ linear}$, has a *O*/*N* ratio of 2 [50]. From these values, the degree of crosslinking was calculated from XPS results using Eq. (2). While the addition of 0.01wt% BNNTs increases the degree of crosslinking from 0.7 to 1.0, this declines moving to 0.02wt% and 0.03wt%, seemingly increasing the density of transport pathways available in selective layer [58].

Table 3 Experimental O/N from XPS and degree of crosslinking.

Membrane	$(O/N)_{XPS}$	$crosslinking$ (%)
PA-BARE	1.3	0.7
PA-BNNTs0.01	1.0	1.0
PA-BNNTs0.02	1.6	0.4
PA-BNNTs0.03	1.7	0.3

3.3 Filtration performance of PA-BNNTs membranes: permeance, rejection and fouling

The permeance of the IP membranes evaluated increases with BNNT loading (Fig. 9a), from an average of 1.1 LMH/bar for the bare membrane to 2.7 LMH/bar for the PA-BNNTs0.01, 4.5 LMH/bar for the PA-BNNTs0.02 and 4.1 LMH/bar for PA-BNNTs0.03. The permeance values hints at a convex profile, often found in literature as a function of loading, as the initial addition of nanomaterial generates an initial increase in pore size, and then a decrease [29]. The former is ascribed to the higher free volume provided by the BNNTs [59], whereas the latter is due to increasing agglomeration [60]. The increase in water flow pathways however does not impact the membrane's rejection performance up to 0.02 wt% loading, most likely because the polyamide layer is still the main contribution to rejection up to that concentration value [59]. This suggests that the addition of the BNNT fillers might have created additional pathways for facile transport of water but not solutes [61, 62], and the slight increase in membrane surface charge might also have contributed to maintain a high rejection [2]. The slight decrease observed in the permeance value from PA-BNNTs0.02 to PA-BNNTs0.03 does not, however, show a statistically significant difference (Student's *t*-test, *p*-value > 0.05).

Two batches of PA-BNNTs membranes (empty and filled symbols in Fig. 9a) were tested for monovalent NaCl and divalent ($CaCl_2$, $MgSO_4$) salts rejection. Calibration curves for these measurements are reported in **Error! Reference source not found.**-4, and ionic concentrations in **Error! Reference source not found.**. The rejection for NaCl remains low (20 – 40 %) for the whole concertation range investigated with 0.03 wt% BNNTs being the worst performing case. However the membranes perform well for divalent salts rejection, with the rejection for $MgSO_4$ is above 90 % for loading up to 0.02 wt% BNNTs, whilst it decreases to ~ 80 % for PA-BNNTs0.03. $CaCl_2$ rejection raises from 75 – 80 % for the bare PA membrane to 97% for the PA-BNNTs0.01 and then decreases to around 40 % with further addition of nanofiller. The mass balance for the rejection of salts was ≥ 96% for $CaCl_2$ and NaCl, and ≥ 90% for $MgSO_4$. In all cases, the addition of 0.03 wt% of BNNTs notably penalises the membranes rejection,

whilst the membranes show highly desirable performances for loadings ≤ 0.02 wt%, with PA-BNNTs0.02, in particular, combining the highest permeance (4.5 LMH/bar) with the highest divalent salt rejection. This is conceivably due to the additional free volume and thus water pathways offered by the presence of the BNNTs in the matrix, while the polyamide enveloping the nanomaterial provides salt rejection.

3.6

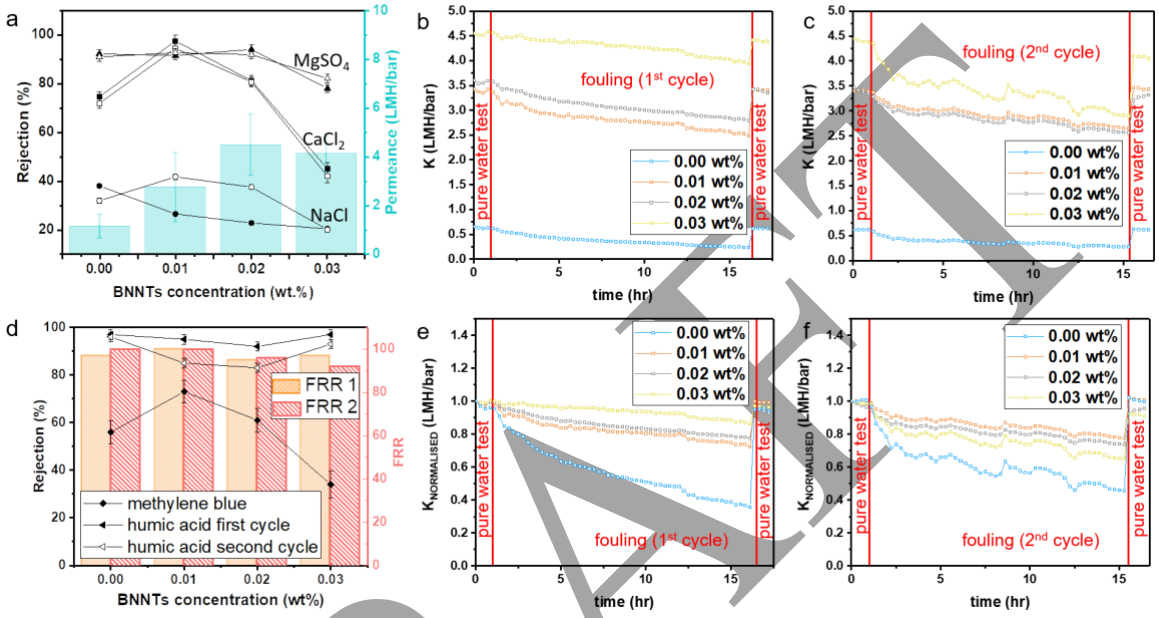

Fig. 9 (a) Salt rejection (left axis) and permeance (right axis) of the bare and TFN membranes containing BNNTs; rejection tests have been repeated on two batches of membranes indicated with full and empty dots for $MgSO_4$, $CaCl_2$ and NaCl: **(b)** First and **(c)** second fouling cycle; **(d)** Rejection of methylene blue (♦) and (◄,◁) humic acid together with flux recovery ratio (FRR) performances in the two fouling cycles in orange and red respectively; **(e)** first and **(f)** second fouling cycle, as displayed in the top panel, but normalised by initial pure water permeance for each membrane tested.

The observed behaviour showed little change in terms of recovering initial flux after two long fouling sequences in Fig. 9b and c, with high FRR: 97%, 100%, 95%, 97 % for the first cycle and 100%, 100%, 96, 92% in the second cycle for PA-BARE, PA-BNNTs0.01, PA-BNNTs0.02 and PA-BNNTs0.03, respectively. The membranes, possessing a white, opaque colour at the start, could be cleaned completely by vigorous water flushing and no irreversible contamination could be observed visually after the test or by the FRR results in the fouling cycles. The pump flow rate chosen in this study (175 ml min^{-1}) is a common setting for membrane fouling tests [26]. However, this behaviour might change if the test was carried out at higher flows, where some irreversible fouling might be observed. However, Fig. 9e and f

explicitly show that PA-BARE reversibly fouls to a greater extent, decreasing to 40% of the initial flux, compared to 80-90% for the TFN membranes. This is possibly due to the absence of repulsion between the fouling material and nanofiller, which may lead to a higher percentage flux decline during tests, even though this is eventually recovered after cleaning. The contribution to total resistance during fouling can be observed in Fig.10.

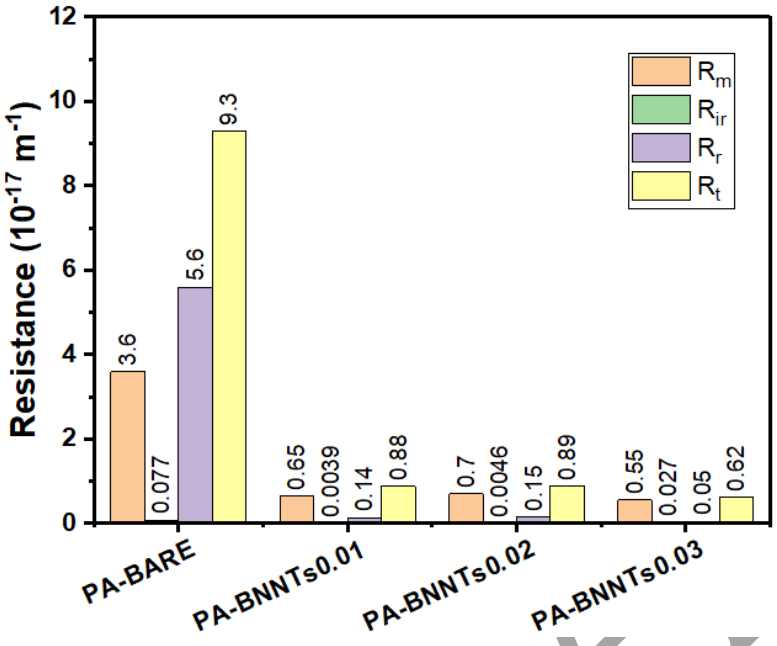

Fig. 10 Calculated membrane (R_m), irreversible (R_{ir}), reversible (R_r) and total (R_t) resistances for the membranes under analysis during the first fouling cycle.

The fouling layer resistance contribution to the total resistance decreased with increased BNNT loading, as indicated by the decrease in value of the parameter $R_{\%}$ for the first fouling cycle from 60.5% for PA-BARE to 8.0% for PA-BNNTs0.03 (**Error! Reference source not found.**). This can be observed in **Error! Reference source not found.** for the second fouling cycle as well, where, however, the benefit in terms of lower fouling layer resistance at high BNNTs loading is attenuated by a slightly lower FRR in PA-BNNTs0.02 and PA-BNNTs0.03.

Fig. 9d shows high rejection (80-90%) of humic acid in all the membranes tested (UV-vis calibration curve reported in **Error! Reference source not found.**). In addition to being able to effectively reject the foulant, all membranes could recover ≥ 95% of their initial flux, with PA-BNNTs0.03 recovering ≥ 90% of its flux after physical cleaning, indicating that the increased membrane roughness can make the removal of the formed fouling layer harder [4].

Fig.9d also reports data on the rejection of methylene blue dye, with the addition of 0.01 wt% BNNTs improving rejection by 17% compared to PA-BARE. Rejection then decreased with

increasing amounts of BNNTs added. As observed in the case of salts, the addition of 0.03 wt% of BNNTs to the thin film worsens rejection performances. The mass balance for the rejection of methylene blue was ≥ 96% for all samples.

The relation between rejection and $CaCl_2$ concentration in the operational range 500 - 2000 ppm was also studied (Fig. 11), with a stable selectivity between 500 and 1500 ppm. Above this value, when Donnan type rejection becomes predominant [63] a decrease in rejection is observed for the PA-BARE and PA-BNNTs0.03, but not for the PA-BNNTs0.01 and PA-BNNTs0.02 for a concentration of $CaCl_2$ of 2000 ppm. When the PA layer is the major contributor to rejection, however, a constant rejection over different concentrations is expected [32]. We can therefore conclude that the PA layer is the major contributor to the rejection of the membranes analysed, for all membranes but PA-BNNTs, where hypothesized defects due to the high loading demonstrate a crucial concern particularly at high concentrations (2000 ppm).

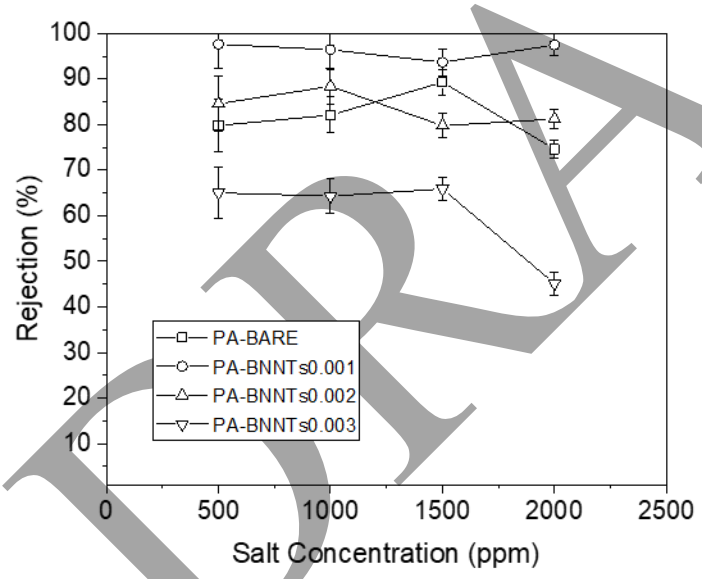

Fig. 11 Dependence of $CaCl_2$ rejection on salt concentration for the membranes analysed in this work.

Membranes based on a polyamide linkage are prone to attack by chlorine in the feed, as free chlorine radicals tend to be attracted by the N-H electron density [2]. Thus, NaOCl exposure is studied here for the membranes under analysis. As observed in Fig. 12, the exposure to the chlorinating agent is more adverse for all PA-BNNTs membranes compared to the PA-BARE, indicating that the introduction of BNNTs in the polyamide structure exposes the amide bonds prone to chlorine attacks. Previously it was found that increasing the density of amide bonds in the PA membrane is a successful strategy for increasing chlorine resistance [64], and this is

consistent with the decrease in crosslinking in the PA-BNNTs membranes leading to premature failure in presence of NaOCl. In fact, at an exposure of 5000 ppm over 1 hr, while $CaCl_2$ rejection of PA-BARE decreased from 89% to 73%, PA-BNNT 0.01wt% plummeted from 97% to 32%. The permeance of PA-BNNTs 0.02wt% increased from 3.67 LMH/bar to 4.68 LMH/bar after 11000 ppm over 1 hr chlorine exposure. However, it remained fairly steady for the other membranes, indicating that the maximum exposure tested did not dissolve the PA layer, but was enough to perturb it and decrease notably its ion rejection.

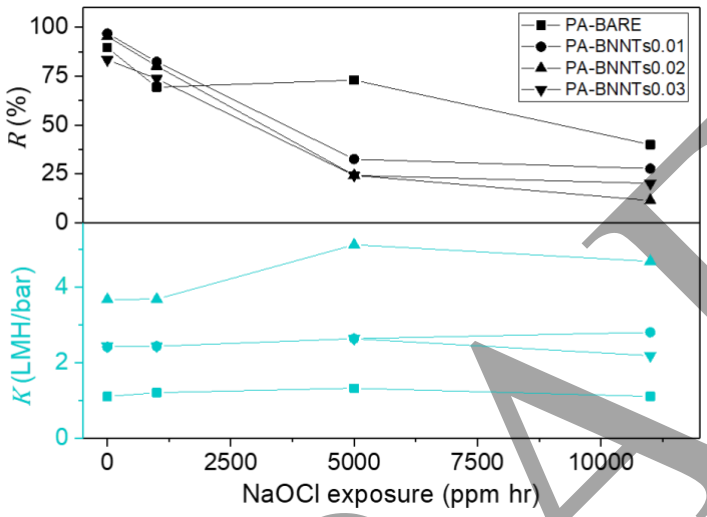

Fig. 12 Rejection (R) of $CaCl_2$ and permeance (K) of PA-BARE, PA-BNNTs0.01, PA-BNNTs0.02 and PA-BNNTs0.03 as a function of the exposure to sodium hypochlorite.

The best performing PA-BNNTs membrane in this work could provide 4 times higher permeance than PA-BARE membranes with only 0.193 mg cm^{-2} of nanofiller on the membrane area. For their part, hydroxyl functionalised CNT membranes were reported to show 2 times higher pure water permeance than thin film polyamide membranes, but required 13.3 mg cm^{-2} of filler [65]. An increase of permeance up to 2.7 times was reported in PA-CNTs, but this required the use of 0.458 mg/cm^2 of modified MWCNTs. When compared with TFN membranes based on CNTs, the membranes in this work have therefore the capability to notably improve the permeance of pure polyamide using a limited amount of nanofiller (**Error! Reference source not found.**) and without requiring any additional functionalisation step.

Conclusions

In this work, a known synthesis route for the production of boron nitride nanotubes was optimised and deployed for the production of larger amounts of boron nitride nanotubes, which were then used as a nanofillers in nanofiltration thin film nanocomposite membranes prepared via interfacial polymerisation of PA. BNNTs homogeneously integrate in the polyamide layer, forming a B-O bond between the nanofiller and the polymer. Rejection of divalent and monovalent salts is not compromised for up to 0.02wt% BNNTs added to the aqueous phase in interfacial polymerisation, while the average permeance at this concentration goes up four times compared to the permeance of a membrane with no nanofiller. This is ascribed to an increase in water transport pathways given by the boron nitride nanochannels enveloped by the selective layer, with no appreciable loss of selectivity compared to the bare PA membrane. A permeance 4.5 times higher than in a bare PA membrane can be observed for low amounts of BNNTs, thus considerably limiting costs of adding nanofillers. Nonetheless, potential nanofiller leaching and recycling will have to be further investigated prior to large scale application, as BNNTs may be hazardous for the environment. In addition, the BNNTs membranes show a high resistance to irreversible fouling. This is a desirable condition for applications in, for example, the food industry, where standard operations take place in highly fouling environments.

Acknowledgments

The Engineering and Physical Sciences Research Council (EPSRC) supported this research under the SynFabFun grant EP/M01486X/1. SC thanks Dr.s Jing Ji and Saeed Mazinani for their very useful suggestions. Many thanks to Prof. Kang Li's group for providing their Planetary Ball Mill for preliminary tests. XPS data collection was performed at the EPSRC National Facility for XPS ('HarwellXPS'), operated by Cardiff University and UCL, under contract No. PR16195. Research data for this work can be accessed at: https://doi.org/10.15125/BATH-00686 .

References

[1] P. Xu, T.Y. Cath, A.P. Robertson, M. Reinhard, J.O. Leckie, J.E. Drewes, Critical review of desalination concentrate management, treatment and beneficial use, Environmental Engineering Science, 30 (2013) 502-514.

[2] J. Yin, B. Deng, Polymer-matrix nanocomposite membranes for water treatment, Journal of membrane science, 479 (2015) 256-275.

[3] E. Jones, M. Qadir, M.T. van Vliet, V. Smakhtin, S.-m. Kang, The state of desalination and brine production: A global outlook, Science of the Total Environment, (2018).

[4] B. Van der Bruggen, C. Vandecasteele, Removal of pollutants from surface water and groundwater by nanofiltration: overview of possible applications in the drinking water industry, Environmental pollution, 122 (2003) 435-445.

[5] M.W. Shahzad, M. Burhan, L. Ang, K.C. Ng, Energy-water-environment nexus underpinning future desalination sustainability, Desalination, 413 (2017) 52-64.

[6] S. Lee, J. Choi, Y.-G. Park, H. Shon, C.H. Ahn, S.-H. Kim, Hybrid desalination processes for beneficial use of reverse osmosis brine: Current status and future prospects, Desalination, 454 (2019) 104-111.

[7] H.B. Park, J. Kamcev, L.M. Robeson, M. Elimelech, B.D. Freeman, Maximizing the right stuff: The trade-off between membrane permeability and selectivity, Science, 356 (2017) eaab0530.

[8] L.Y. Ng, A.W. Mohammad, C.P. Leo, N. Hilal, Polymeric membranes incorporated with metal/metal oxide nanoparticles: a comprehensive review, Desalination, 308 (2013) 15-33.

[9] W. Lau, A. Ismail, N. Misdan, M. Kassim, A recent progress in thin film composite membrane: a review, Desalination, 287 (2012) 190-199.

[10] S. Hermans, R. Bernstein, A. Volodin, I.F. Vankelecom, Study of synthesis parameters and active layer morphology of interfacially polymerized polyamide–polysulfone membranes, Reactive and Functional Polymers, 86 (2015) 199-208.

[11] Z. Fan, Z. Wang, N. Sun, J. Wang, S. Wang, Performance improvement of polysulfone ultrafiltration membrane by blending with polyaniline nanofibers, Journal of Membrane Science, 320 (2008) 363-371.

[12] Y. Mansourpanah, S. Madaeni, A. Rahimpour, M. Adeli, M. Hashemi, M. Moradian, Fabrication new PES-based mixed matrix nanocomposite membranes using polycaprolactone modified carbon nanotubes as the additive: property changes and morphological studies, Desalination, 277 (2011) 171-177.

[13] H. Zhao, L. Wu, Z. Zhou, L. Zhang, H. Chen, Improving the antifouling property of polysulfone ultrafiltration membrane by incorporation of isocyanate-treated graphene oxide, Physical Chemistry Chemical Physics, 15 (2013) 9084-9092.

[14] E.M. Hoek, A.K. Ghosh, X. Huang, M. Liong, J.I. Zink, Physical–chemical properties, separation performance, and fouling resistance of mixed-matrix ultrafiltration membranes, Desalination, 283 (2011) 89-99.

[15] S. Zhao, Z. Wang, X. Wei, X. Tian, J. Wang, S. Yang, S. Wang, Comparison study of the effect of PVP and PANI nanofibers additives on membrane formation mechanism, structure and performance, Journal of membrane science, 385 (2011) 110-122.

[16] J.M. Arsuaga, A. Sotto, G. del Rosario, A. Martínez, S. Molina, S.B. Teli, J. de Abajo, Influence of the type, size, and distribution of metal oxide particles on the properties of nanocomposite ultrafiltration membranes, Journal of membrane science, 428 (2013) 131-141.

[17] P. Daraei, S.S. Madaeni, N. Ghaemi, E. Salehi, M.A. Khadivi, R. Moradian, B. Astinchap, Novel polyethersulfone nanocomposite membrane prepared by PANI/Fe3O4 nanoparticles

with enhanced performance for Cu (II) removal from water, Journal of Membrane Science, 415 (2012) 250-259.

[18] A. Rahimpour, S. Madaeni, A. Taheri, Y. Mansourpanah, Coupling TiO2 nanoparticles with UV irradiation for modification of polyethersulfone ultrafiltration membranes, Journal of Membrane Science, 313 (2008) 158-169.

[19] A. Berezhkovskii, G. Hummer, Single-file transport of water molecules through a carbon nanotube, Phys Rev Lett, 89 (2002) 064503.

[20] S. Casanova, M.K. Borg, Y.J. Chew, D. Mattia, Surface-controlled water flow in nanotube membranes, ACS applied materials & interfaces, 11 (2018) 1689-1698.

[21] M. Elimelech, W.A. Phillip, The future of seawater desalination: energy, technology, and the environment, science, 333 (2011) 712-717.

[22] D. Mattia, H. Leese, K.P. Lee, Carbon nanotube membranes: from flow enhancement to permeability, Journal of Membrane Science, 475 (2015) 266-272.

[23] M. Majumder, N. Chopra, B.J. Hinds, Effect of Tip Functionalization on Transport through Vertically Oriented Carbon Nanotube Membranes, J. Am. Chem. Soc., 127 (2005) 9062-9070.

[24] K.P. Lee, T.C. Arnot, D. Mattia, A review of reverse osmosis membrane materials for desalination—development to date and future potential, Journal of Membrane Science, 370 (2011) 1-22.

[25] M. Baghbanzadeh, D. Rana, C.Q. Lan, T. Matsuura, Effects of inorganic nano-additives on properties and performance of polymeric membranes in water treatment, Separation & Purification Reviews, 45 (2016) 141-167.

[26] Z.-X. Low, J. Ji, D. Blumenstock, Y.-M. Chew, D. Wolverson, D. Mattia, Fouling resistant 2D boron nitride nanosheet – PES nanofiltration membranes, Journal of Membrane Science, 563 (2018) 949-956.

[27] F. Xiao, B. Wang, X. Hu, S. Nair, Y. Chen, Thin film nanocomposite membrane containing zeolitic imidazolate framework-8 via interfacial polymerization for highly permeable nanofiltration, Journal of the Taiwan Institute of Chemical Engineers, 83 (2018) 159-167.

[28] H. Zhao, S. Qiu, L. Wu, L. Zhang, H. Chen, C. Gao, Improving the performance of polyamide reverse osmosis membrane by incorporation of modified multi-walled carbon nanotubes, Journal of Membrane Science, 450 (2014) 249-256.

[29] J. Yin, G. Zhu, B. Deng, Multi-walled carbon nanotubes (MWNTs)/polysulfone (PSU) mixed matrix hollow fiber membranes for enhanced water treatment, Journal of membrane science, 437 (2013) 237-248.

[30] C.C. Yu, H.W. Yu, Y.X. Chu, H.M. Ruan, J.N. Shen, Preparation thin film nanocomposite membrane incorporating PMMA modified MWNT for nanofiltration, in: Key Engineering Materials, Trans Tech Publ, 2013, pp. 882-886.

[31] H. Wu, B. Tang, P. Wu, MWNTs/polyester thin film nanocomposite membrane: an approach to overcome the trade-off effect between permeability and selectivity, The Journal of Physical Chemistry C, 114 (2010) 16395-16400.

[32] W.-F. Chan, H.-y. Chen, A. Surapathi, M.G. Taylor, X. Shao, E. Marand, J.K. Johnson, Zwitterion functionalized carbon nanotube/polyamide nanocomposite membranes for water desalination, Acs Nano, 7 (2013) 5308-5319.

[33] J. Park, W. Choi, S.H. Kim, B.H. Chun, J. Bang, K.B. Lee, Enhancement of chlorine resistance in carbon nanotube based nanocomposite reverse osmosis membranes, Desalination and Water Treatment, 15 (2010) 198-204.

[34] D. Golberg, Y. Bando, Y. Huang, T. Terao, M. Mitome, C. Tang, C. Zhi, Boron nitride nanotubes and nanosheets, ACS nano, 4 (2010) 2979-2993.

[35] M. Suk, A. Raghunathan, N. Aluru, Fast reverse osmosis using boron nitride and carbon nanotubes, Applied Physics Letters, 92 (2008) 133120.

[36] C.Y. Won, N. Aluru, Water permeation through a subnanometer boron nitride nanotube, Journal of the American Chemical Society, 129 (2007) 2748-2749.

[37] E. Secchi, S. Marbach, A. Niguès, D. Stein, A. Siria, L. Bocquet, Massive radius-dependent flow slippage in carbon nanotubes, Nature, 537 (2016) 210-213.

[38] J. Sokoloff, Enhancement of the water flow velocity through carbon nanotubes resulting from the radius dependence of the friction due to electron excitations, Physical Review E, 97 (2018) 033107.

[39] T.A. Hilder, D. Gordon, S.H. Chung, Salt rejection and water transport through boron nitride nanotubes, Small, 5 (2009) 2183-2190.

[40] A. Siria, P. Poncharal, A.-L. Biance, R. Fulcrand, X. Blase, S.T. Purcell, L. Bocquet, Giant osmotic energy conversion measured in a single transmembrane boron nitride nanotube, Nature, 494 (2013) 455.

[41] H. Lim, B.L. Suh, M.J. Kim, H. Yun, J. Kim, B.J. Kim, S.G. Jang, High-performance, recyclable ultrafiltration membranes from P4VP-assisted dispersion of flame-resistive boron nitride nanotubes, Journal of membrane science, 551 (2018) 172-179.

[42] X. Lin, Q. Yang, L. Ding, B. Su, Ultrathin silica membranes with highly ordered and perpendicular nanochannels for precise and fast molecular separation, ACS nano, 9 (2015) 11266-11277.

[43] C.H. Lee, J. Wang, V.K. Kayatsha, J.Y. Huang, Y.K. Yap, Effective growth of boron nitride nanotubes by thermal chemical vapor deposition, Nanotechnology, 19 (2008) 455605.

[44] M. Crimp, D. Oppermann, K. Krehbiel, Suspension properties of hexagonal BN powders: effect of pH and oxygen content, Journal of materials science, 34 (1999) 2621-2625.

[45] R.Y. Tay, H. Li, S.H. Tsang, L. Jing, D. Tan, M. Wei, E.H.T. Teo, Facile Synthesis of Millimeter-Scale Vertically Aligned Boron Nitride Nanotube Forests by Template-Assisted Chemical Vapor Deposition, Chemistry of Materials, 27 (2015) 7156-7163.

[46] K.P. Lee, J. Zheng, G. Bargeman, A.J. Kemperman, N.E. Benes, pH stable thin film composite polyamine nanofiltration membranes by interfacial polymerisation, Journal of membrane science, 478 (2015) 75-84.

[47] G. Lai, W. Lau, P. Goh, Y. Tan, B. Ng, A. Ismail, A novel interfacial polymerization approach towards synthesis of graphene oxide-incorporated thin film nanocomposite membrane with improved surface properties, Arabian journal of chemistry, (2017).

[48] R.N. Wenzel, Surface roughness and contact angle, The Journal of Physical Chemistry, 53 (1949) 1466-1467.

[49] B. Liu, S. Yan, Z. Song, M. Liu, X. Ji, W. Yang, J. Liu, One-step synthesis of boron nitride quantum dots: Simple chemistry meets delicate nanotechnology, Chemistry–A European Journal, 22 (2016) 18899-18907.

[50] C.Y. Tang, Y.-N. Kwon, J.O. Leckie, Probing the nano-and micro-scales of reverse osmosis membranes—A comprehensive characterization of physiochemical properties of uncoated and coated membranes by XPS, TEM, ATR-FTIR, and streaming potential measurements, Journal of Membrane Science, 287 (2007) 146-156.

[51] A. Celik-Aktas, J.-M. Zuo, J.F. Stubbins, C. Tang, Y. Bando, Double-helix structure in multiwall boron nitride nanotubes, Acta Crystallographica Section A: Foundations of Crystallography, 61 (2005) 533-541.

[52] B.J. Hinds, N. Chopra, T. Rantell, R. Andrews, V. Gavalas, L.G. Bachas, Aligned multiwalled carbon nanotube membranes, Science, 303 (2004) 62-65.

[53] T. Chen, J. Xiao, G. Yang, Cubic boron nitride with an intrinsic peroxidase-like activity, RSC Advances, 6 (2016) 70124-70132.

[54] N. Saha, S. Joshi, Performance evaluation of thin film composite polyamide nanofiltration membrane with variation in monomer type, Journal of Membrane Science, 342 (2009) 60-69.

[55] F. Mirabella Jr, Practical spectroscopy series, Internal Reflection Spectroscopy: Theory and Applications, (1993) 17-52.

[56] B. Zhong, X. Huang, G. Wen, H. Yu, X. Zhang, T. Zhang, H. Bai, Large-scale fabrication of boron nitride nanotubes via a facile chemical vapor reaction route and their cathodoluminescence properties, Nanoscale Res Lett, 6 (2011) 36.

[57] W. Laosamathikul, T. Sawada, T. Serizawa, Alcoholysis-Assisted Exfoliation of Boron Nitride Nanosheets from Hexagonal Boron Nitride, Transactions of the Materials Research Society of Japan, 42 (2017) 135-138.

[58] M.L. Lind, D. Eumine Suk, T.-V. Nguyen, E.M. Hoek, Tailoring the structure of thin film nanocomposite membranes to achieve seawater RO membrane performance, Environmental science & technology, 44 (2010) 8230-8235.

[59] S. Roy, S.A. Ntim, S. Mitra, K.K. Sirkar, Facile fabrication of superior nanofiltration membranes from interfacially polymerized CNT-polymer composites, Journal of Membrane Science, 375 (2011) 81-87.

[60] J.S. Taurozzi, C.A. Crock, V.V. Tarabara, C60-polysulfone nanocomposite membranes: entropic and enthalpic determinants of C60 aggregation and its effects on membrane properties, Desalination, 269 (2011) 111-119.

[61] B.-H. Jeong, E.M. Hoek, Y. Yan, A. Subramani, X. Huang, G. Hurwitz, A.K. Ghosh, A. Jawor, Interfacial polymerization of thin film nanocomposites: a new concept for reverse osmosis membranes, Journal of membrane science, 294 (2007) 1-7.

[62] J. Yin, E.-S. Kim, J. Yang, B. Deng, Fabrication of a novel thin-film nanocomposite (TFN) membrane containing MCM-41 silica nanoparticles (NPs) for water purification, Journal of membrane science, 423 (2012) 238-246.

[63] F. Fornasiero, H.G. Park, J.K. Holt, M. Stadermann, C.P. Grigoropoulos, A. Noy, O. Bakajin, Ion exclusion by sub-2-nm carbon nanotube pores, Proceedings of the National Academy of Sciences, 105 (2008) 17250-17255.

[64] S.G. Kim, D.H. Hyeon, J.H. Chun, B.-H. Chun, S.H. Kim, Nanocomposite poly (arylene ether sulfone) reverse osmosis membrane containing functional zeolite nanoparticles for seawater desalination, Journal of membrane science, 443 (2013) 10-18.

[65] S.-M. Xue, Z.-L. Xu, Y.-J. Tang, C.-H. Ji, Polypiperazine-amide nanofiltration membrane modified by different functionalized multiwalled carbon nanotubes (MWCNTs), ACS applied materials & interfaces, 8 (2016) 19135-19144.

[66] H.-Z. Zhang, Z.-L. Xu, H. Ding, Y.-J. Tang, Positively charged capillary nanofiltration membrane with high rejection for Mg2+ and Ca2+ and good separation for Mg2+ and Li+, Desalination, 420 (2017) 158-166.

[67] J. nan Shen, C. chao Yu, H. min Ruan, C. jie Gao, B. Van der Bruggen, Preparation and characterization of thin-film nanocomposite membranes embedded with poly (methyl methacrylate) hydrophobic modified multiwalled carbon nanotubes by interfacial polymerization, Journal of membrane science, 442 (2013) 18-26.